# High-Fidelity Aerodynamic Shape Optimization of a Full Configuration Regional Jet

Nicolas P. Bons[*], Charles A. Mader[†], Joaquim R. R. A. Martins[‡]
*University of Michigan, Department of Aerospace Engineering, Ann Arbor, MI*
Felipe I. K. Odaguil[§], Ana P. C. Cuco[¶]
*Embraer - São José dos Campos, São Paulo*

**Gradient-based optimization with high-fidelity aerodynamic modeling is used to analyze and improve the design of a 100 passenger regional jet. The full configuration of the jet, including wing, body, tail, pylon, and nacelle components, is considered in this optimization. Overset meshing is used to allow component independence in the meshing scheme and in the geometry parametrization. We analyze the tradeoffs between wing shape, altitude, and engine size and consider the impact of adding constraints such as climb rate, takeoff field length, and buffet onset margin. The final optimized design achieves a 2% improvement over the baseline while satisfying these constraints.**

## 1. Introduction

The maturation of the jet age has been marked by the rise of new design objectives that motivate continuing innovation in aircraft design. An increased awareness in the public conscience of the negative consequences of fossil fuel emissions has created a demand for cleaner, more efficient air travel [1]. The cost of fuel itself is another incentive to make aircraft more fuel-efficient. Restrictions on jet engine noise add yet another constraint to the design problem. To address these needs, a great deal of research has been invested in the creation of novel aircraft concepts that will allow a step increase in performance. These include blended-wing body, truss-braced wing, and double-bubble designs. On the other hand, the need for incremental improvements to conventional tube-and-wing designs has pushed researchers to capitalize on ever-smaller details to maximize performance.

Multidisciplinary design optimization (MDO) has emerged as an indispensable tool for exploiting trade-offs and finding the optimal design for a given mission. The most realistic result can be obtained by simultaneously optimizing the structure and the aerodynamic shape of the aircraft, so that the optimizer can find the optimal compromise between competing interests [2]. The merits of aerostructural optimization are apparent with both low-fidelity [3, 4] and high-fidelity [5–7] analyses.

Significant improvements can be made when optimizing with respect to a single discpline as well. Aerodynamic shape optimization has been applied to the design of wings [8, 9], winglets [10, 11], and wing-body intersections [12, 13]. Additionally, novel configurations such as the blended-wing-body [14, 15] and D8 double-bubble [16] have been optimized to improve aerodynamic performance. As the complexity of the design increases, there is a greater likelihood that the optimizer will be able to expose interactions between different facets of the design and make improvements. Leaving pieces of the design out of the optimization not only prevents improvement of those parts, but can also decrease the synergistic improvement made possible by the coupling between disparate parts. For example, in an optimization of an over-wing nacelle design, there is a strong interaction between wing shape and nacelle position that can not be exploited if only the nacelle is optimized [17].

Despite the large body of work covering the optimization of aircraft design, there has not been a high-fidelity optimization study of a full configuration aircraft considering wing, nacelle, pylon, fuselage, and tail. Toubin et al. [18] and Fang et al. [19] looked at the optimization of a nacelle by itself. Koc et al. [20] conducted optimization of a wing-body-nacelle-pylon configuration with low-fidelity CFD analysis and Smith et al. [21] did the same, but with the addition of a post-optimization viscous shape correction which was used as a substitute while the capability for direct viscous-flow shape optimization was being developed. Our hypothesis is that there are additional trade-offs to be understood from optimizing the wing shape with RANS CFD analysis while considering the effects on the full configuration.

---

[*]Ph.D. Candidate, AIAA Student Member.
[†]Research Investigator, AIAA Senior Member.
[‡]Professor, AIAA Associate Fellow.
[§]Product Engineer, AIAA Member.
[¶]Research Engineer, AIAA Member.

Additionally, we will investigate the effect of varying altitude and engine size on fuel burn. These additional variables allow us to consider mission-relevant constraints such as climb rate, takeoff and landing field length, and buffet onset margin.

## 2.    Methodology

### 2.1.    Aircraft Specifications

The aircraft under consideration is a 100 passenger regional jet. The baseline geometry consists of a fuselage, wing with winglet, underwing pylon and nacelle, and empennage. More details can be found in Table 1.

**Table 1.  Aircraft Specifications**

| | | |
|---|---|---|
| Wingspan | $b$ | 28.72 m |
| Reference area | $S$ | 95.4 m$^2$ |
| Maximum takeoff weight | MTOW | 51,800 kg |

### 2.2.    Optimization Framework

We conduct the optimizations in this study using the MDO of aircraft configurations with high fidelity (MACH) framework [22]. The development of this framework has been catalogued in several publication over the last decade, some of which are cited in the following descriptions. For the present work, we have made a few new additions and their salient characteristics are described herein.

#### 2.2.1.    Optimizer

Gradient-based optimization is suited for problems with large sets of design variables. All of the MACH framework is differentiated using a combination of analytic and algorithmic differentiation in order to provide the optimizer with accurate gradient information. We use SNOPT [23], wrapped in pyOptSparse, as our optimizer because it is especially suited to sparse, nonlinear optimization problems.

#### 2.2.2.    Geometric Parametrization

The MACH framework utilizes the free-form deformation (FFD) method [24] to change the shape of the geometry. An FFD volume is a grid structure defined and controlled by B-spline control points. The surface mesh representation of the geometry is embedded inside the FFD volume and assumes any deformations applied to it. The geometric design variables, depicted in Figure 1, control the design via displacement of the FFD control points. The twist design variables rotate the wing sections about the quarter-chord. In each spanwise section of the wing FFD, the control points are perturbed in a uniform direction set perpendicularly to the wing surface. This particular incarnation of the FFD method, wrapped in a module called pyGeo, computes derivatives of the embedded points with respect to the design variables with the complex-step method.

#### 2.2.3.    CFD Solver

The flow solver in MACH is ADflow, a finite-volume CFD solver for cell-centered multiblock and overset meshes. ADflow solves the compressible Euler, laminar Navier–Stokes, and RANS equations with a second-order accurate spatial discretization. For this study, we use RANS analysis in order to provide the optimizer with accurate predictions of the aerodynamic performance of the aircraft.

#### 2.2.4.    Mesh Generation

The outer mold line (OML) of the aircraft is represented using overset meshes. Each component of the aircraft has its own surface mesh representation (see Fig. 2), which is used to extrude a volume mesh. All of the volume meshes are combined together with a far-field mesh in an implicit-hole cutting process. In this process, interpolation cells are designated to transfer information between the individual meshes. This enables a more modular meshing process and also opens up the possibility of optimizing the intersections between components, as done by Secco et al. [12].
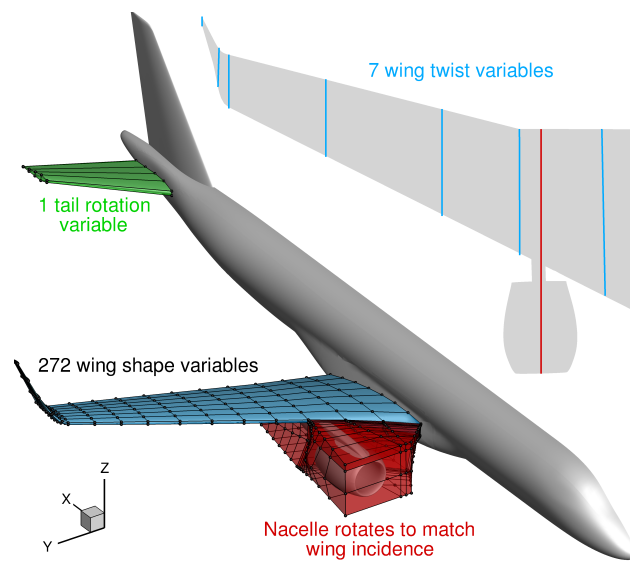
**Figure 1. The wing shape is parametrized with 7 twist variables and 272 shape variables. The nacelle rotates with no shape deformation to match the rotation at its spanwise junction with the wing. The tail rotates with no shape deformation to provide trim control to the optimizer.**
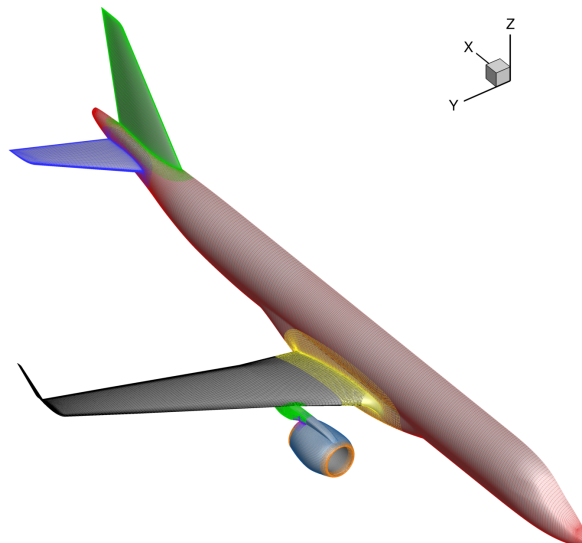


**Figure 2. Individual component surface meshes.**
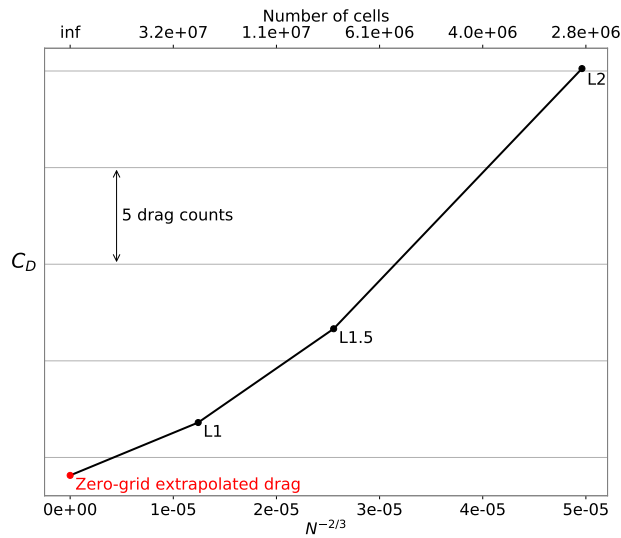
American Institute of Aeronautics and Astronautics

**Figure 3. Grid convergence study. All grids were trimmed at $C_L = 0.44$. The L2 mesh (2,860,946 cells) was used for all optimization results.**

### 2.2.5. Mesh Warping

Any deformations of the surface mesh due to design variable changes are propagated to the volume mesh via an unstructured mesh warping algorithm [24].

### 2.2.6. Conceptual Aerodynamic Analysis

Some of the design constraints considered in this work are related to field performance criteria like takeoff field length (TOFL) and landing field length (LFL). These constraints require some prediction of the aerodynamic performance of the aircraft in high-lift configuration. Since we do not have a high-fidelity model of the high-lift devices, we opt to use conceptual-level, parameter-based formulas from common aircraft design references to estimate lift and drag for these conditions. This approach is not expected to yield accurate predictions, but it is intended to capture the trends due to changing geometric parameters. The novelty of our approach is that we are able to maintain the FFD parametrization as a means of adjusting the geometric parameters relevant to the conceptual formulas. Airfoil slices of the baseline wing geometry are discretized and then embedded in the FFD along with the high-fidelity surface mesh points. Geometric parameters such as span, reference area, and leading-edge radius are then computed based on the positions of these points and any displacement of the points is reflected in an adjustment to the parameter value.

The functions of interest include the coefficients of parasitic drag and maximum lift with high-lift devices deployed. Parasitic drag is computed using the component buildup method suggested by Raymer [25], wherein the drag of each component is a function of wetted area, the flat-plate skin friction coefficient, a form factor, and an interference factor. The computation of $C_{L_{\max}}$ is based on the method described by Finck [26], of which the key geometric parameters are leading edge radius, flap and slat areas, wing sweep, and thickness-to-chord ratio.

Like everything else in the MACH framework, the fundamental philosophy in developing this capability was to allow for efficient, accurate derivative computation. The derivatives of the functions of interest with respect to the geometric parameters are analytically derived and the derivatives of the geometric parameters with respect to the airfoil points are computed with the complex-step method. The derivatives of the points with respect to the design variables are already handled in pyGeo, and in the end, derivatives of the functions of interest with respect to the design variables are obtained by combining the three different sets.

### 2.2.7. Engine Model

The engine performance is represented using a surrogate model built from engine data of thrust and fuel consumption with respect to true airspeed, altitude, and temperature. We use a surrogate model from the Surrogate Modeling Toolbox (SMT) [27] called Regularized minimal-energy tensor-product splines (RMTS) [28]. SMT is especially suited to gradient-based optimization because it provides analytic gradients of the functions of interest with respect

to the independent variables. The relationship between engine fuel consumption and throttle setting is modeled as a quartic polynomial based on engine data. All of the engine data was provided by Embraer.

## 2.3. Optimization Problem

The objective is to minimize the average fuel burn of three representative missions, weighted as follows:

$$\overline{FB} = w_1 FB_{NOM} + w_2 FB_{HS} + w_3 FB_{LR} \tag{1}$$

where $w_1 > w_2 > w_3$. Mission details can be found in Table 2. The fuel burn for each of these missions is computed as the difference in weight from takeoff ($W_0$) to landing ($W_5$), where the basic mission profile is defined as indicated in Figure 4. Fuel fractions are used to compute fuel burn over the taxi/takeoff, climb, descent, and landing phases of the mission. The cruise fuel burn is approximated using the Breguet range equation,

$$R = \frac{V}{c_t} \frac{L}{D} \ln \frac{W_2}{W_3} \tag{2}$$

which can be simply rearranged as

$$\frac{W_2}{W_3} = \exp\left(\frac{c_t R D}{V L}\right) \tag{3}$$

where $c_t$ is thrust-specific fuel consumption. Lift, drag, and thrust-specific fuel consumption are computed for each cruise mission at the mid-cruise weight
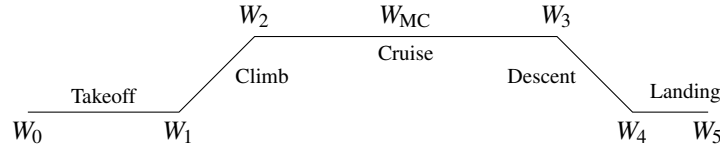
$$W_{MC} = \frac{W_2 + W_3}{2} \tag{4}$$



**Figure 4. Basic mission profile.**

**Table 2. Mission details**

| Code | Description | Range (nm) | Mach | Payload (kg) |
|------|-------------|-----------:|------|-------------:|
| NOM | Nominal | 600 | 0.78 | 10,000 |
| LR | Long-range | 1000 | 0.74 | 10,000 |
| HS | High-speed | 300 | 0.80 | 10,000 |
| MTOW | Maximum takeoff weight | TBD | 0.78 | 11,000 |
| DEN | Takeoff from Denver at ISA+28°C | 1200 | 0.78 | 10,000 |
| SF | Takeoff from short field | 500 | 0.78 | 10,000 |

The design is constrained to satisfy various aircraft performance requirements during the optimization. First, the aircraft must not exceed the takeoff and landing field distances of the baseline design under certain critical conditions. For takeoff performance, these conditions include maximum takeoff weight (MTOW), hot and high takeoff from Denver airport, and takeoff from a short field. The critical weight for the landing field length constraint is 80% MTOW. The formulas for takeoff and landing distance come from Raymer [25] and Anderson [29].

Additional design constraints are enforced on the cruise performance of the aircraft. The altitude at which all missions are flown is allowed to vary, but the rate of climb at the beginning of cruise for the high-speed and MTOW missions is constrained to be at least 300 feet per minute. Rate of climb is computed as

$$RC = \frac{V(T - D)}{W_2} \tag{5}$$

We also enforce buffet onset constraints at the start of cruise for the MTOW mission after the manner of Kenway et al. [30]. This ensures a safe buffet margin in the case of a 1.3$g$ maneuver or an increase in speed up to Mach 0.82.

**Table 3. Optimization problem matrix**

| | | Optimization Cases | | | | | |
|---|---|---|---|---|---|---|---|
| | | 1 | 2 | 3 | 4 | 5 | 6 |
| | High-fidelity analysis points | | | | | | |
| | Nominal cruise | • | • | • | • | • | • |
| | Long-range cruise | • | • | • | • | • | • |
| | High-speed cruise | • | • | • | • | • | • |
| | Cruise from MTOW for maximum range | | | • | • | • | • |
| | Cruise from Denver | | | • | | | • |
| | Cruise from short field | | | • | | | • |
| | Top of climb at high-speed | | | | • | | |
| | Top of climb from MTOW | | | | • | | • |
| | 1.3$g$ top of climb from MTOW | | | | | • | • |
| | Mach 0.82 top of climb from MTOW | | | | | • | |
| | Function/Variable | | | Quantity | | | |
| minimize | $\overline{\text{FB}}$ | | | ——— 1 ——— | | | |
| with respect to | Altitude | | 1 | 1 | 1 | 1 | 1 |
| | Angle of attack for all analysis points | 3 | 3 | 6 | 6 | 6 | 8 |
| | Tail rotation angle for all analysis points | 3 | 3 | 6 | 6 | 6 | 8 |
| | Engine throttle for all cruise analysis points | 3 | 3 | 6 | 4 | 4 | 6 |
| | Engine size | | 1 | 1 | 1 | 1 | 1 |
| | Wing twist | | | ——— 7 ——— | | | |
| | Wing local shape variables | | | ——— 272 ——— | | | |
| | **Total number of design variables** | **288** | **290** | **299** | **297** | **297** | **303** |
| subject to | $L = W_{\text{MC}}$ for all cruise analysis points | 3 | 3 | 6 | 4 | 4 | 6 |
| | $L = W_2$ for top of climb analysis points | | | | 2 | 1 | 1 |
| | $L = 1.3W_2$ for 1.3$g$ buffet analysis point | | | | | 1 | 1 |
| | $C_{M_y} = 0$ for all analysis points | 3 | 3 | 6 | 6 | 6 | 8 |
| | $D = T$ for all cruise analysis points | 3 | 3 | 6 | 4 | 4 | 6 |
| | $RC \geq 300\,\text{fpm}$ | | | | 2 | | 1 |
| | Takeoff field length limit | | | 3 | | | 3 |
| | Landing field length limit | | | 1 | | | 1 |
| | MTOW maximum range limit | | | 1 | | | 1 |
| | Buffet constraint | | | | | 2 | 1 |
| | Thickness contraints | | | ——— 260 ——— | | | |
| | LE/TE constraints (prevent shearing twist) | | | ——— 46 ——— | | | |
| | **Total number of design constraints** | **315** | **315** | **329** | **329** | **329** | **335** |

# 3. Results

**Case 1**

In the first case, we maintain altitude and engine size constant and concern ourselves solely with achieving the most efficient flying shape to minimize fuel burn. As seen in Figure 5, the optimizer removes the majority of the shock above the wing by flattening out the pressure distribution over the upper surface of the wing. The optimal design also reduces the incidence angle inboard of the nacelle significantly, pushing the load distribution further out on the wing. This is expected since we are giving no consideration to the structural integrity of the wing, and thus the optimizer wants to remove the heavy load borne by the inboard wing in favor of achieving a more favorably distributed loading. Table 4 presents the percentage difference of the optimized result from the baseline configuration. The optimized design burns 1.4% less fuel over the three missions due to significant increases in $L/D$ for the Nominal and Long-range design points. The decrease in drag during cruise means that the engines must be throttled to produce less thrust and the optimized design is actually cruising at a less efficient throttle setting than the baseline. However, the improvement in $L/D$ is enough to offset the increase in TSFC. Making the engine size a variable in subsequent cases allows the optimizer to tune the throttle settings so that improvements in drag performance are not detrimental to engine performance.
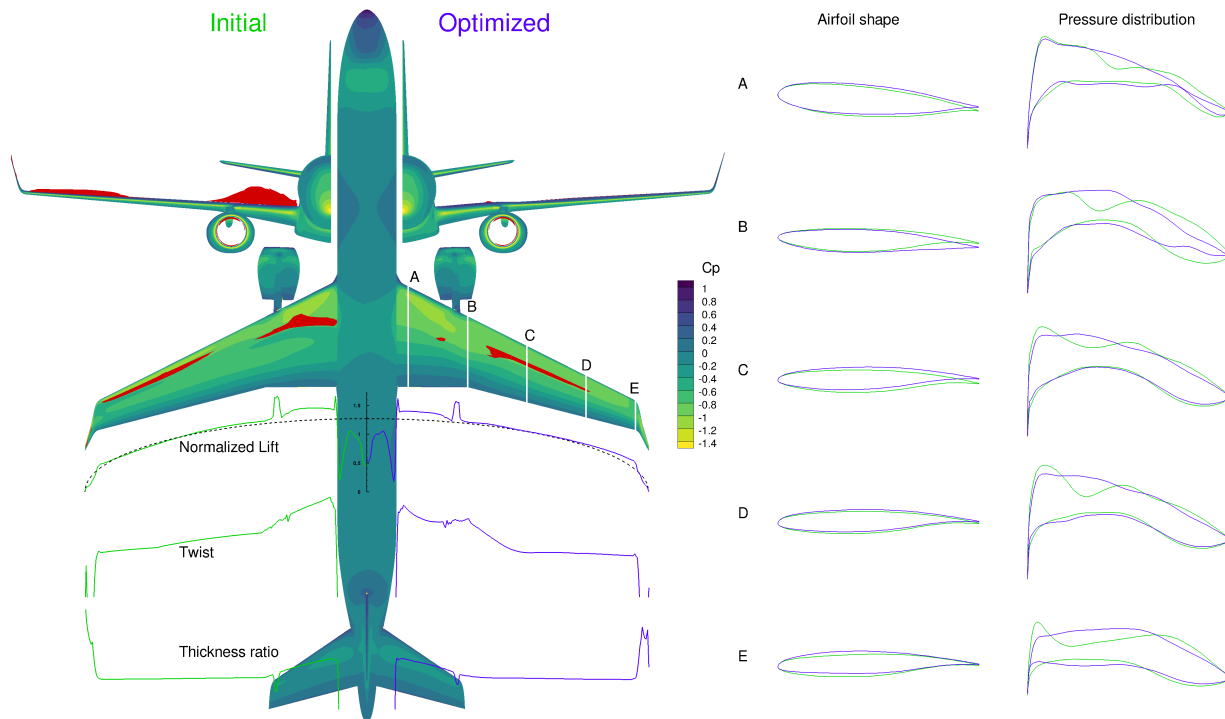


**Figure 5. Comparison of initial and optimized designs for Case 1. Average fuel burn decreases by 1.4%. The contours and distributions pertain to the Nominal cruise design point.**

**Case 2**

In Case 2 we give the optimizer control over the cruise altitude and engine size without adding additional constraints. From Equation 3, fuel burn can be minimized by decreasing drag, improving $c_T$, or by flying higher. In this case, the optimizer takes advantage of all three of these areas. The altitude goes to its upper bound of 40,000 ft. This behavior of prioritizing the maximization of altitude is persistent across the cases where altitude is a variable. Lower density at higher altitude means that the aircraft must fly at a higher lift coefficient to generate enough lift to offset its weight. Although this does increase lift-induced drag, which scales quadratically with the lift coefficient, the overall decrease in drag due to lower density results in a significant gain in $L/D$. The engine size is tailored to move the throttle setting deeper into the trough where minimum thrust-specific fuel consumption is found. As expected, based on the relative weights used in the fuel-burn averaging, the fuel efficiency in the Nominal and Long-range missions is prioritized above that of the High-speed mission. Figure 6 shows the shifts along the thrust bucket curves that reuslt in a net decrease in specific fuel consumption for the Nominal and Long-range missions at the expense of an increase in the

**Table 4. Quantitative optimization results. Unless otherwise noted, values are listed as percentage difference from the trimmed baseline configuration.**

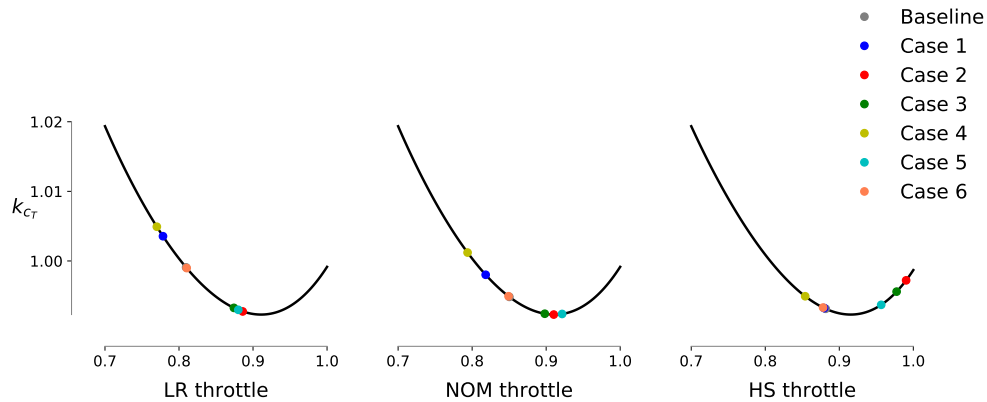| Optimization Case | 1 | 2 | 3 | 4 | 5 | 6 |
|---|---|---|---|---|---|---|
| Objective | −1.4 | −3.5 | −3.6 | −3.0 | −2.2 | −2.0 |
| $FB_{NOM}$ | −1.6 | −4.1 | −4.1 | −2.9 | −2.3 | −2.1 |
| $FB_{LR}$ | −2.1 | −4.5 | −4.5 | −3.6 | −3.1 | −2.7 |
| $FB_{HS}$ | 0.0 | −0.7 | −0.7 | −0.8 | −0.9 | −0.9 |
| $L/D_{NOM}$ | 3.8 | 9.2 | 9.3 | 8.6 | 4.7 | 4.5 |
| $L/D_{LR}$ | 3.8 | 6.9 | 7.0 | 6.7 | 4.4 | 4.3 |
| $L/D_{HS}$ | 0.2 | 4.2 | 4.2 | 4.7 | 4.6 | 4.8 |
| $c_{t,NOM}$ | 0.3 | −0.2 | −0.2 | 0.7 | −0.3 | −0.1 |
| $c_{t,LR}$ | 0.4 | −0.5 | −0.5 | 0.7 | −0.6 | −0.1 |
| $c_{t,HS}$ | 0.0 | 0.5 | 0.3 | 0.2 | 0.0 | −0.1 |
| Altitude (ft) | 36,000 | 40,000 | 40,000 | 40,000 | 38,235 | 37,977 |
| Engine size factor | 1.00 | 1.01 | 1.03 | 1.17 | 0.96 | 1.04 |
| $RC$ at $W_{2,MTOW}$ (fpm) | 408 | - | - | 300 | −3 | 300 |



**Figure 6. Change in thrust-specific fuel consumption based on throttle setting. The factor $k_{c_T}$ is multiplied by the full-throttle value of $c_T$ to get the throttled value.**

American Institute of Aeronautics and Astronautics

same quantity for the High-speed mission. Finally, Figure 7 shows similar improvements to Case 1 in reducing the shock and adjusting the lift distribution.
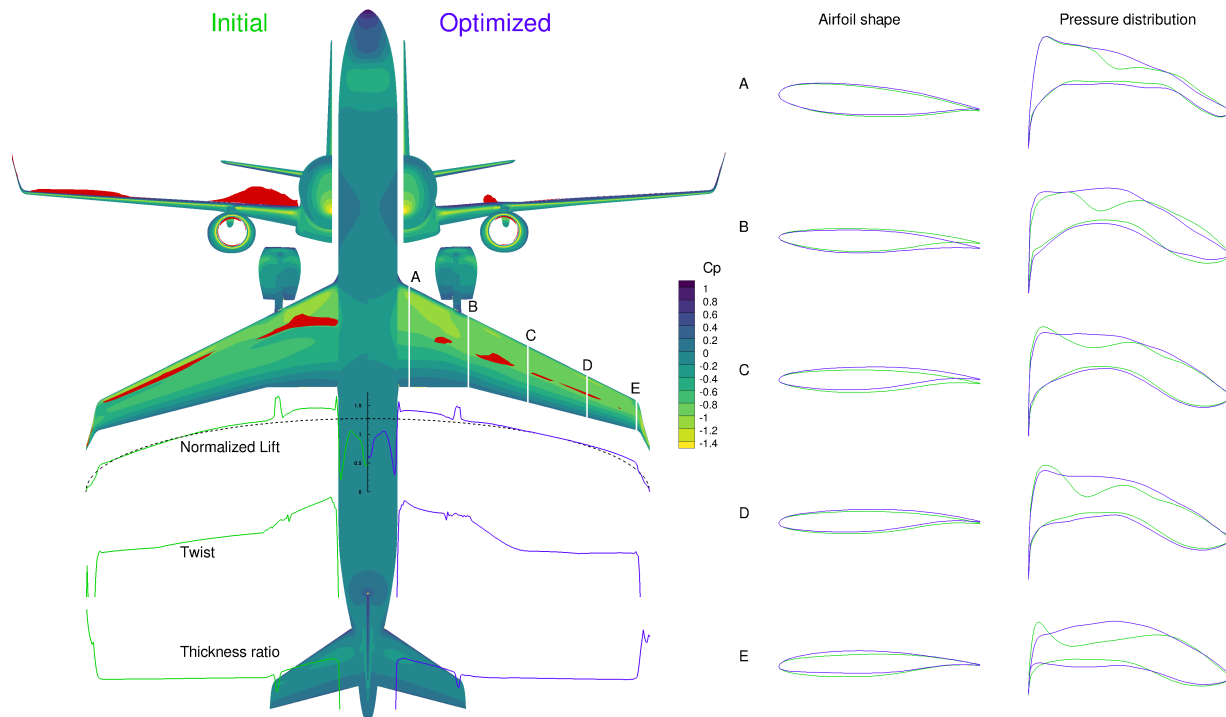


**Figure 7. Comparison of initial and optimized designs for Case 2. Average fuel burn decreases by 3.5%. The contours and distributions pertain to the Nominal cruise design point.**

## Case 3

In Case 3 we add the field constraints into the optimization problem. The field performance is mainly dependent on $C_{L_{max}}$ and engine thrust. Because the current parametrization does not allow changes in the planform shape of the wing, the changes in $C_{L_{max}}$ are minor and the satisfaction of the field constraints dominated by engine sizing. Since the engine size increases slightly to achieve better cruise performance, the takeoff field lengths are slightly decreased and none of the field performance constraints are active. The landing field length remains basically the same as the baseline configuration. Figure 9 shows a comparison of field performance between the different cases. We note that an important tradeoff is neglected here due to the fact that engine weight is considered fixed and independent of the engine sizing variable. The final result is basically the same result as Case 2, with any discrepancies due to a flat design space near the optimum.

## Case 4

In Case 4 the High-speed and MTOW design points are constrained to have a minimum residual climb rate of 300 feet per minute at the beginning of cruise. The High-speed rate-of-climb constraints remain inactive during the optimization, but the MTOW rate-of-climb constraint forces a substantial increase in engine size. The optimizer still goes to the maximum allowable cruise altitude, despite the fact that this requires nearly a 30% larger engine and sets the throttle for the Long-range, Nominal, and High-speed cruise points far from the location for minimum $c_T$. The cost of the larger engine is that Case 4 achieves only a 2.5% decrease in fuel burn compared to 3.5% for Cases 2 and 3. However, even with the added rate-of-climb constraints, Case 4 fares better than Case 1, where no changes in altitude were allowed, because of the overwhelming gains in $L/D$ possible from cruising at a higher altitude.

## Case 5

In all of the foregoing cases where altitude is a variable, the optimizer pushes the altitude to the upper limit to capitalize on the improved $L/D$, even when this means decreasing engine efficiency. In Case 5, we test the practicality of cruising at such a high altitude by adding two buffet onset constraints at the beginning of cruise on the MTOW design point.
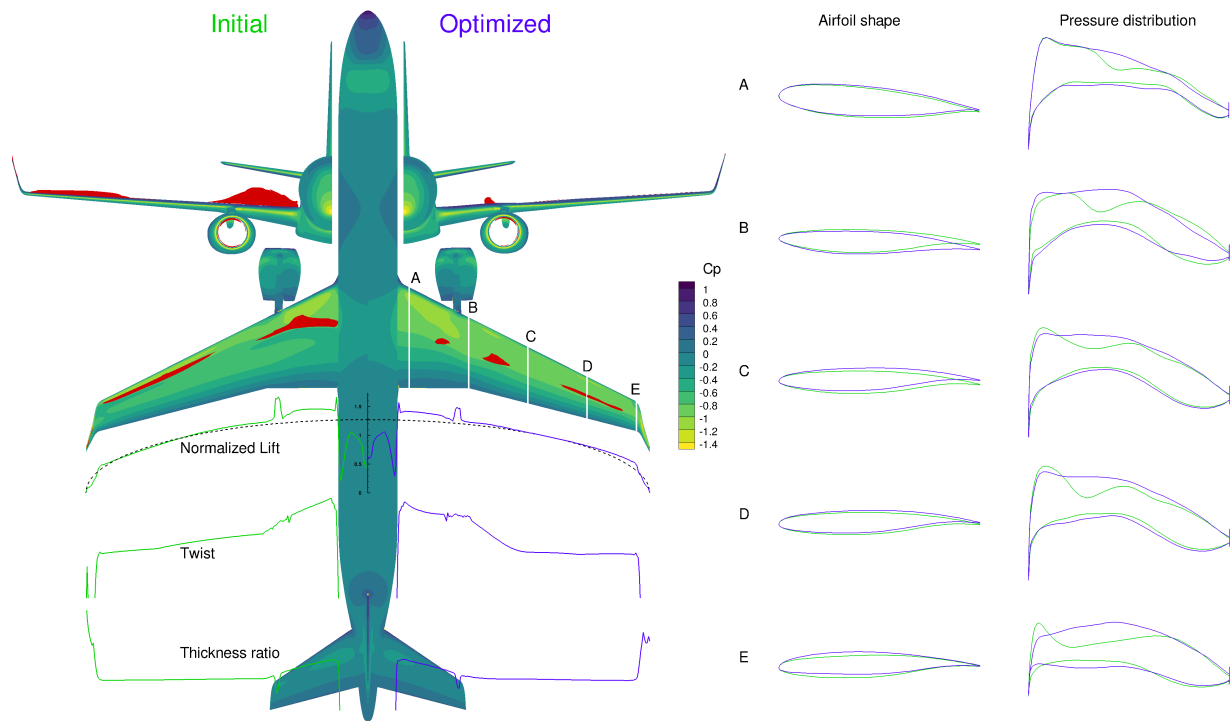
**Figure 8. Comparison of initial and optimized designs for Case 3, where field performance constraints are considered. Average fuel burn decreases by 3.6%. The contours and distributions pertain to the Nominal cruise design point.**
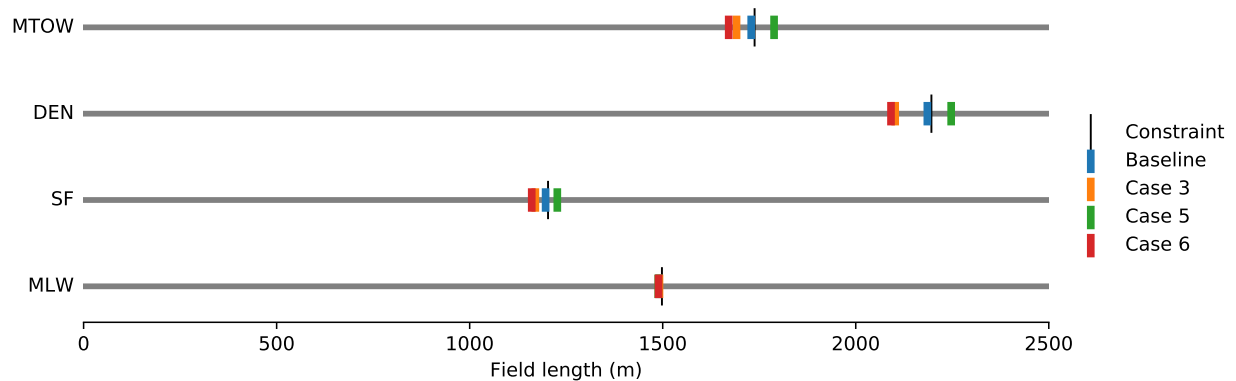


**Figure 9. Visualization of the four field performance constraints. The top three axes correspond to the takeoff field lengths of the MTOW, Denver, and Short-field design points, respectively. The final axis shows the landing field length at maximum landing weight. The constraints, indicated by the thin black vertical lines, were set 0.05% above the baseline value.**

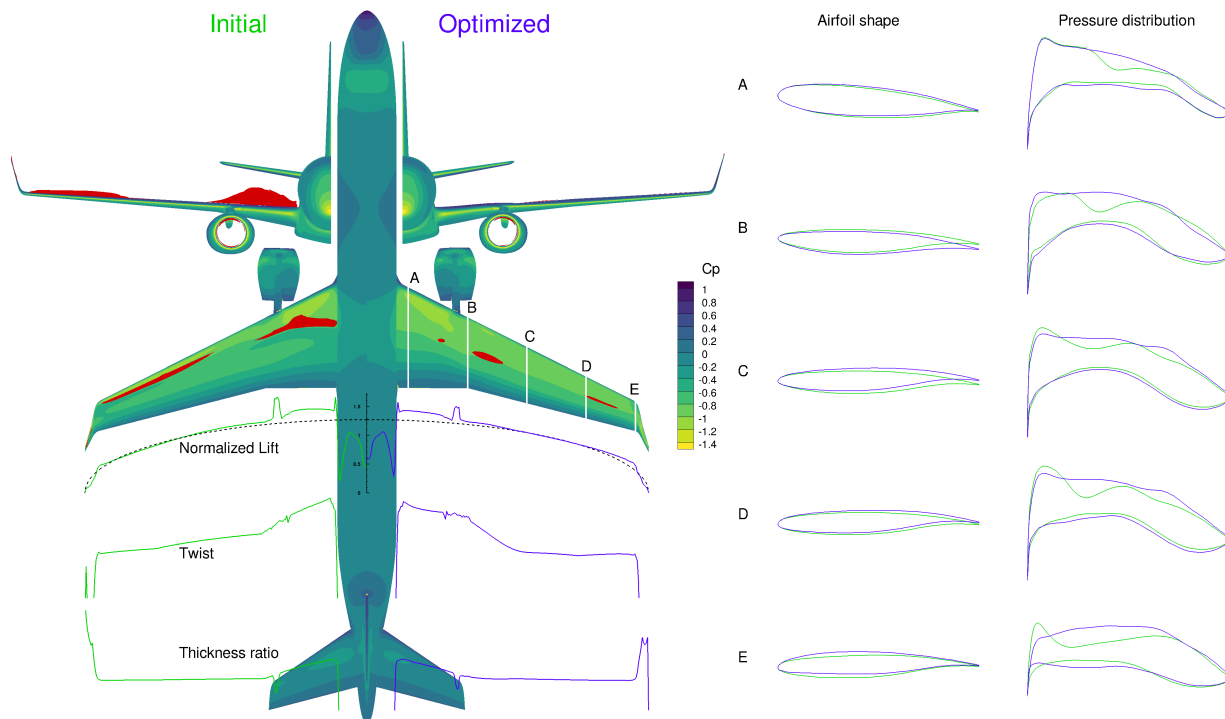American Institute of Aeronautics and Astronautics

**Figure 10. Comparison of initial and optimized designs for Case 4, where climb rate constraints are considered. Average fuel burn decreases by 3%. The contours and distributions pertain to the Nominal cruise design point.**

The first buffet onset constraint is applied for a 1.3$g$ condition and the second is applied for a slight increase in speed to Mach 0.82. The latter constraint remains inactive in the optimization but the former is active, resulting in a decrease in the cruise altitude of about 1,800 feet. Due to the fact that the rate-of-climb constraint was not applied in this case, the engine size is actually scaled down 4% from the baseline, allowing the throttle settings for each of the fuel burn design points to settle close to the optimal efficiency. As seen in Table 4, the rate of climb at beginning of the cruise segment for the MTOW mission is actually negative, meaning that the scaled-down engine is not powerful enough to maintain the desired altitude. Although field performance constraints were not applied in this case, the smaller engine does not provide enough power to satisfy them, as shown in Figure 9. This provides motivation to pay the extra cost of including both field and climb rate constraints in the optimization.

**Case 6**

The sixth and final optimization is a combination of cases 3, 4, and 5. We include the field constraints, the rate-of-climb constraint on the MTOW design point, and the 1.3$g$ buffet onset constraint. Both the climb rate and buffet constraints are active in the optimization, however the field constraints remain inactive. The altitude decreases from Case 5 by about 250 feet and the engine size is scaled up by 3.6% from the baseline. This demonstrates once again the great benefit of cruising at a higher altitude, even if it means increasing the engine size to satisfy the climb constraint. Although the rate-of-climb constraint was dominant in this case, this does not invalidate the importance of considering field constraints. As Case 5 shows, the field constraints would come into play to restrict excessive shrinking of the engines if the rate-of-climb constraint was not present. In this case, due to the limited design space considered, the two constraints are basically linked to the same variables and logically, only one of them should be active.

## 4. Conclusion

We optimized the wing shape of a 100 passenger regional jet to minimize fuel burn averaged over three different missions. When only wing shape variables and trim variables are exposed, the optimizer achieves a 1.4% decrease in the average fuel burn. When the optimizer is allowed to vary the cruise altitude, the optimal solution invariably sits at the maximum allowable altitude. This increase in cruise altitude occurs even when an increase in engine size is required to satisfy rate-of-climb constraints at the beginning of cruise. Field constraints do not affect the solution because we are not giving the optimizer control over the aspects of the geometry (i.e. planform area, sweep) that have
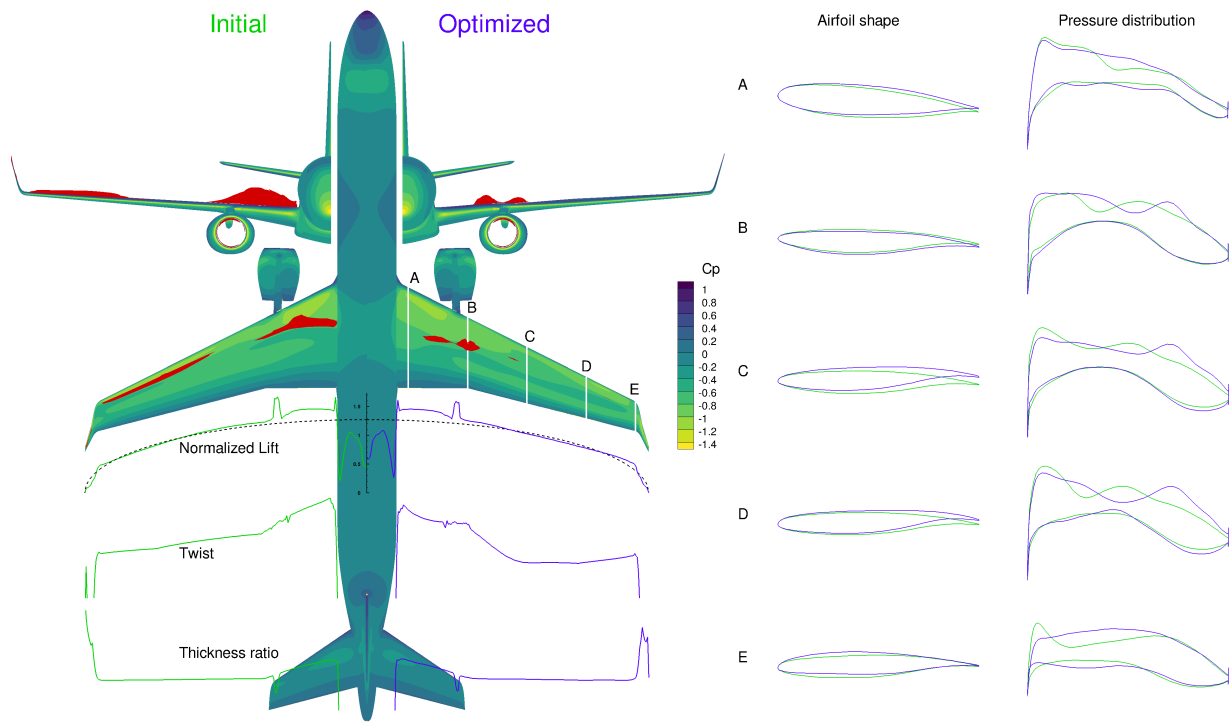
American Institute of Aeronautics and Astronautics

**Figure 11.** Comparison of initial and optimized designs for Case 5. Average fuel burn decreases by 2.2%. The contours and distributions pertain to the Nominal cruise design point.
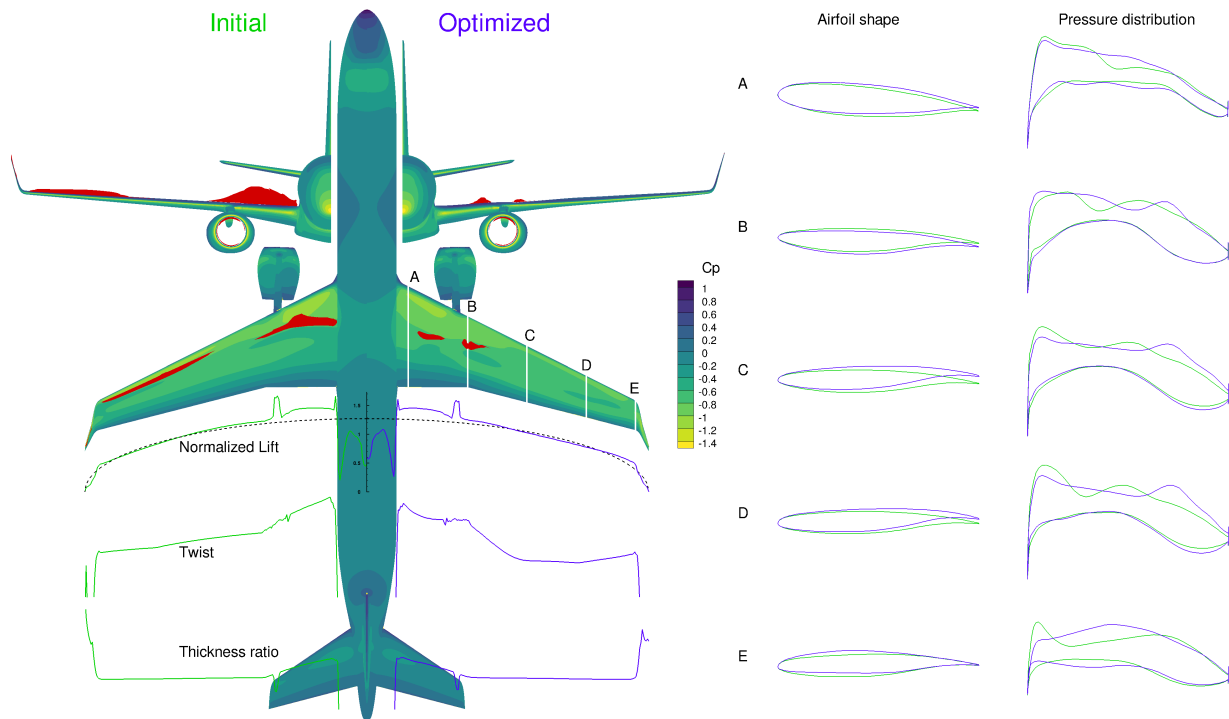


**Figure 12.** Comparison of initial and optimized designs for Case 6. Average fuel burn decreases by 2%. The contours and distributions pertain to the Nominal cruise design point.

American Institute of Aeronautics and Astronautics

a major influence on $C_{L_{\max}}$. The application of a buffet onset constraint at the beginning of cruise for the MTOW mission prevents the altitude from approaching the upper limit. The combination of these design constraints results in a more practical optimal design that is still able to achieve better performance than the baseline configuration. We expect that the full benefit of developing this case study for high-fidelity analysis will be realized as we open up the design space to planform changes.

## 5.   Acknowledgements

## References

[1] Lee, D. S., Fahey, D. W., Forster, P. M., Newton, P. J., Wit, R. C., Lim, L. L., Owen, B., and Sausen, R., "Aviation and global climate change in the 21st century," *Atmospheric Environment*, Vol. 43, No. 22-23, Jul 2009, pp. 3520–3537.

[2] Kenway, G. K. W., Kennedy, G. J., and Martins, J. R. R. A., "Scalable Parallel Approach for High-Fidelity Steady-State Aeroelastic Analysis and Adjoint Derivative Computations," *AIAA Journal*, Vol. 52, No. 5, May 2014, pp. 935–951.

[3] Haftka, R. T., "Optimization of flexible wing structures subject to strength and induced drag constraints," *AIAA Journal*, Vol. 15, No. 8, Aug 1977, pp. 1101–1106.

[4] Jansen, P. W., Perez, R. E., and Martins, J. R. R. A., "Aerostructural optimization of nonplanar lifting surfaces," *Journal of Aircraft*, Vol. 47, No. 5, 2010, pp. 1490–1503.

[5] Brooks, T. R., Kennedy, G. J., and Martins, J. R. R. A., "High-fidelity Multipoint Aerostructural Optimization of a High Aspect Ratio Tow-steered Composite Wing," *58th AIAA/ASCE/AHS/ASC Structures, Structural Dynamics, and Materials Conference*, 2017, p. 1350.

[6] Burdette, D. A., Kenway, G. K. W., and Martins, J. R. R. A., "Aerostructural design optimization of a continuous morphing trailing edge aircraft for improved mission performance," *17th AIAA/ISSMO Multidisciplinary Analysis and Optimization Conference*, 2016, p. 3209.

[7] Liem, R. P., Kenway, G. K. W., and Martins, J. R. R. A., "Multimission Aircraft Fuel-Burn Minimization via Multipoint Aerostructural Optimization," *AIAA Journal*, Vol. 53, No. 1, Jan 2015, pp. 104–122.

[8] Hicks, R. M. and Henne, P. A., "Wing Design by Numerical Optimization," *Journal of Aircraft*, Vol. 15, No. 7, 1978, pp. 407–412.

[9] Lyu, Z., Kenway, G. K. W., and Martins, J. R. R. A., "Aerodynamic shape optimization investigations of the common research model wing benchmark," *AIAA Journal*, Vol. 53, No. 4, 2014, pp. 968–985.

[10] Pfeiffer, N., "Numerical winglet optimization," *42nd AIAA Aerospace Sciences Meeting and Exhibit*, 2004, p. 213.

[11] Khosravi, S. and Zingg, D. W., "A numerical optimization study on winglets," *15th AIAA/ISSMO Multidisciplinary Analysis and Optimization Conference*, 2014, p. 2173.

[12] Secco, N. R., Jasa, J., Kenway, G. K., and Martins, J., "Component-based Geometry Manipulation for Aerodynamic Shape Optimization with Overset Meshes," *18th AIAA/ISSMO Multidisciplinary Analysis and Optimization Conference*, Jun 2017.

[13] Mykhaskiv, O., Mohanamuraly, P., Müller, J.-D., Xu, S., and Timme, S., "CAD-based shape optimisation of the NASA CRM wing-body intersection using differentiated CAD-kernel," *35th AIAA Applied Aerodynamics Conference*, 2017, p. 4080.

[14] Lyu, Z. and Martins, J. R. R. A., "Aerodynamic Design Optimization Studies of a Blended-Wing-Body Aircraft," *Journal of Aircraft*, Vol. 51, No. 5, Sep 2014, pp. 1604–1617.

[15] Reist, T. A. and Zingg, D. W., "High-Fidelity Aerodynamic Shape Optimization of a Lifting-Fuselage Concept for Regional Aircraft," *Journal of Aircraft*, Vol. 54, No. 3, May 2017, pp. 1085–1097.

[16] Mader, C. A., Kenway, G. K., Martins, J., and Uranga, A., "Aerostructural Optimization of the D8 Wing with Varying Cruise Mach Numbers," *18th AIAA/ISSMO Multidisciplinary Analysis and Optimization Conference*, Jun 2017.

[17] Berguin, S. and Mavris, D., "Interactions in Over-Wing Nacelle Optimization," *51st AIAA Aerospace Sciences Meeting including the New Horizons Forum and Aerospace Exposition*, Jan 2013.

[18] Toubin, H., Salah El Din, I., and Meheut, M., "Multipoint Aerodynamic High Fidelity Shape Optimization of an Isolated Engine Nacelle," *52nd Aerospace Sciences Meeting*, 2014, p. 0903.

[19] Fang, X., Zhang, Y., Li, S., and Chen, H., "Transonic Nacelle Aerodynamic Optimization Based on Hybrid Genetic Algorithm," *17th AIAA/ISSMO Multidisciplinary Analysis and Optimization Conference*, Jun 2016.

[20] Koc, S., Kim, H. J., and Nakahashi, K., "Aerodynamic Design of Wing-Body-Nacelle-Pylon Configuration," *17th AIAA Computational Fluid Dynamics Conference*, Jun 2005.

[21] Smith, S., Nemec, M., and Krist, S., "Integrated Nacelle-Wing Shape Optimization for an Ultra-High Bypass Fanjet Installation on a Single-Aisle Transport Configuration," *51st AIAA Aerospace Sciences Meeting including the New Horizons Forum and Aerospace Exposition*, Jan 2013.

[22] Kenway, G. K. W. and Martins, J. R. R. A., "Multipoint High-Fidelity Aerostructural Optimization of a Transport Aircraft Configuration," *Journal of Aircraft*, Vol. 51, No. 1, Jan 2014, pp. 144–160.

[23] Gill, P. E., Murray, W., and Saunders, M. A., "An SQP algorithm for large-scale constrained optimization," *Society for Industrial and Applied Mathematics*, Vol. 47, No. 1, 2005.

[24] Kenway, G. K. W., Kennedy, G. J., and Martins, J. R. R. A., "A CAD-free approach to high-fidelity aerostructural optimization," *13th AIAA/ISSMO multidisciplinary analysis optimization conference*, 2010, p. 9231.

[25] Raymer, D. P., *Aircraft Design: A Conceptual Approach*, AIAA, 5th ed., 2012.

[26] Finck, R., (US), A. F. F. D. L., and Hoak, D., *USAF stability and control DATCOM*, Engineering Documents, 1978.

[27] Bouhlel, M. A. and Hwang, J. T., "Surrogate Modeling Toolbox," Nov 2017.

[28] Hwang, J. T. and Martins, J. R. R. A., "A fast-prediction surrogate model for large datasets," *Aerospace Science and Technology*, 2017.

[29] Anderson, Jr, J. D., *Aircraft Performance and Design*, McGraw–Hill, 1999.

[30] Kenway, G. K. and Martins, J. R., "Buffet-Onset Constraint Formulation for Aerodynamic Shape Optimization," *AIAA Journal*, 2017.

American Institute of Aeronautics and Astronautics